Experimental and Numerical Study of the Hydraulic Analogy to Supersonic Flow

***Ziyaad Arendze*[1] *and Beric W. Skews*[2]**

Received 26 October 2007, in revised form 18 March 2008 and accepted 12 May 2008

A qualitative and quantitative study of the hydraulic analogy between flow with a free surface and two dimensional compressible gas flow is described. The experimentation was done using a water table, and results are compared with computational fluid dynamic (CFD) results for free surface flow models, a fictitious gas model, and analytical solutions for flow over a wedge. Three steady flow Mach numbers are considered as well as unsteady motion of a wedge accelerating to supercritical speeds and then decelerating. Quantitative results for the experimental case are achieved by using a colour encoding slope detection technique. Qualitatively, with respect to wave angles, the fictitious gas case shows the best agreement to the experimental case, but at higher Froude/Mach numbers the free surface models also show good agreement. Quantitatively, with respect to wave location and depth profile, the free surface models show better agreement with the experimental case. For the unsteady case the resulting flow patterns are quite similar for the two cases considered, i.e. the experimental and free surface CFD cases.

Nomenclature

Roman

c	wave propagation velocity [m/s]
d	water depth [m]
Fr	Froude number
g	acceleration due to gravity [m/s^2]
M	Mach number
p/p_0	Pressure ratio
T/T_0	Temperature ratio

Greek

γ	specific heat ratio
λ	wavelength [m]
ρ	density [kg/m^3]
σ	surface tension [N/m^2]

1. Introduction

The hydraulic analogy has been known for some time with Mach[1] first commenting on it, while the mathematical development by Jouget[2] followed a few years later. The analogy has been applied to a wide variety of problems in gas dynamics. More recently, methods of quantitative visualization techniques have been pursued. Presently, computational fluid dynamics (CFD) software has enabled shallow water flow to be modelled, thereby adding an additional tool to examine the analogue. The mathematical formulation for the analogue is well summarised by Orlin[3]. The main parameters are given in table 1 where the 0 subscript refers to the undisturbed flow ahead of the wave system.

2d gas flow	Water flow
Density ratio ρ/ρ	Water depth ratio d/d_0
Temperature ratio T/T_0	Water depth ratio d/d_0
Pressure ratio p/p_0	Square of depth ratio $(d/d_0)^2$
Velocity of sound a	Wave velocity $(gd)^{0.5}$
Mach number M	Froude number Fr
Shock wave	Hydraulic jump

Table 1: Analogue parameters

The analysis identifies restrictions on the application of the analogy for quantitative work. The analogy applies only to a perfect gas with a ratio of specific heats $\gamma = 2$, and neither air nor any other gas has this value. An inherent assumption that the flow is isentropic is also not valid for discontinuities. Actual fluid effects are not considered in the development of the analogy, and are different for the two types of flow. The actual propagation velocity of a surface wave in water is given by[4,5]

$$c = \sqrt{\left(\frac{g\lambda}{2\pi} + \frac{2\pi\sigma}{\rho\lambda}\right)\tanh\frac{2\pi d}{\lambda}} \tag{1}$$

where σ is the surface tension and λ the wavelength. If d/λ is large, tanh $(2\pi d/\lambda)$ tends towards 1. If d/λ is small tanh $(2\pi d/\lambda)$ tends towards $2\pi d/\lambda$ and the wave speed simplifies to

$$c = \sqrt{gd} \tag{2}$$

which represents the propagation speed of the gravity waves. The second term in the braces of equation 1 represents the smaller capillary waves. The surface wave is the sum of all wavelengths. In general the propagation velocity decreases with wavelength, due to the capillary waves, and increases again due to gravity. The height at which the tanh term compensates the height at which the water is rising, can be found. This would mean that at this height the propagation speed is constant with wavelength, and outside the capillary wave region. This height is calculated to be 4.7 mm, but it is concluded that a height between 4 mm and 6 mm is acceptable[6]. Extensive research has been done to determine the optimal height. Black[7] found this height to be 0.5 inches but suggested that a depth of 1 inch should be used since the boundary layer will be a proportionally smaller part of the measured depth. Orlin[3] compared flow patterns around a cylinder at different depths to that in a high speed wind tunnel and found the best agreement to be for depths between 0.75 inches and 1 inch.

Certain effects also have no counterpart in the gaseous case. Effects such as bottom flow boundary layers, the periodicity of gravity waves, and that there are two types of hydraulic jumps;

---

[1] University of the Witwatersrand, now Aerosud Aviation (Pty) Ltd.

[2] FSAIMechE, Flow Research Unit, School of Mechanical, Industrial and Aeronautical Engineering, University of the Witwatersrand, Johannesburg.
E-mail: beric.skews@wits.ac.za

undular and regular. Additional restrictions apply when there are vertical perturbations in the initial conditions[8]. Nevertheless, an attraction of the method is also due to the fact that the ratio of velocity of sound in air to the velocity of propagation of gravity waves in shallow water, which are analogous, is a factor of one thousand, and thus transient events are slowed down a thousand times.

Notwithstanding the restrictions of the method, and besides its simplicity in demonstrating wave patterns, it has significant potential for use in the study of unsteady flows, many of which cannot be done in conventional high-speed wind tunnel facilities. Consider for example the case of a manoeuvring aircraft. It would be a simple matter to use a water table to explore, for example, the two-dimensional wave pattern resulting from a non-linear flight trajectory, before undertaking more sophisticated techniques. Even the case of acceleration in a straight line cannot be done in a wind tunnel because of the fundamental differences in the flow fields between a stationary body surrounded by an accelerating flow, and an accelerating body in a stationary field. This paper aims to explore comparisons between water table experiments, computational solutions to the shallow water equation, the analytical perfect gas solution for the fictitious $\gamma = 2$ gas, and a CFD solution for the same case, with a view to extending the method to unsteady flow cases.

2. Facilities and Methods

2.1 The water table

A general view of the apparatus is shown in figure 1. The surface over which the water flows consists of a slab of glass with dimensions 1.97 m in the streamwise direction and 1.5 m wide. Water is pumped from a reservoir into an upstream settling chamber, passes over the glass sheet into a collection channel from where it is returned to the reservoir. For static testing (i.e. a stationary model) either the flow rate is increased or the tilt of the table is changed in order to change the flow velocity at a desired water depth. For dynamic testing when the model is moved at variable speed or follows an arbitrary trajectory, the water table is kept horizontal with a thin layer of stationary water and no external water supply. A rail and pulley system is used to move the model in the present case of linear motion.

An aluminium wedge was used for the tests. The wedge has a 20° apex angle, a chord of 113 mm and a thickness of 30 mm.

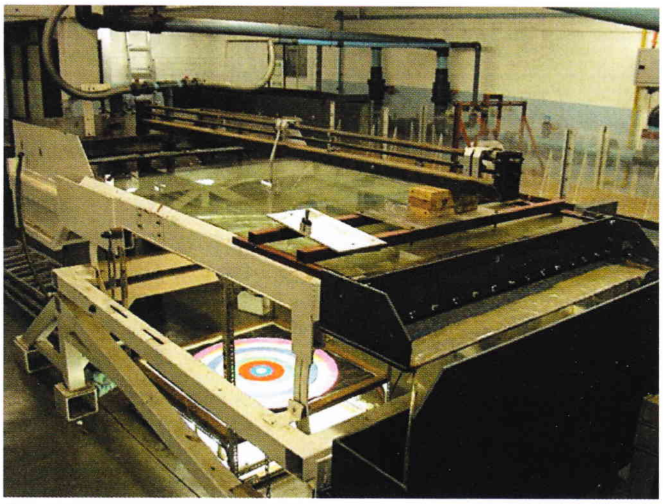

Figure 1: The water table facility

2.2 Visualisation and water height measurement

A colour-coded method of visualising a free surface water table flow and from which water depth variation can be determined has been described by Skews[9]. It is based on the method of Zhang and Cox[10] which they applied to oceanographic flows. The principle of operation is illustrated in figure 2 (the glass sheet of the table is left out of the sketch for clarity, but refraction through it also needs to be accounted for). The camera is positioned as far from the water surface as practicable so that only vertical rays can enter it. Consider the colour mask to be made of a series of concentric circles of different colours scattering light upwards. If the colour is blue at the optical axis, at A, a collimated beam of blue light is created through the lens, rays of which will only enter the camera if the water surface slope is zero, such as for rays AC and AD. However, the blue ray AB will be bent away from the camera at the inclined water surface. If the colour mask at E is green then a green ray EG is refracted by the water surface into the camera, while rays EF and EH will bypass the camera. Thus a pattern of coloured bands will be recorded by the camera with each band identifying a value of the water surface slope. A major advantage of this technique is that the gradient distribution over the entire surface is defined from a single image.

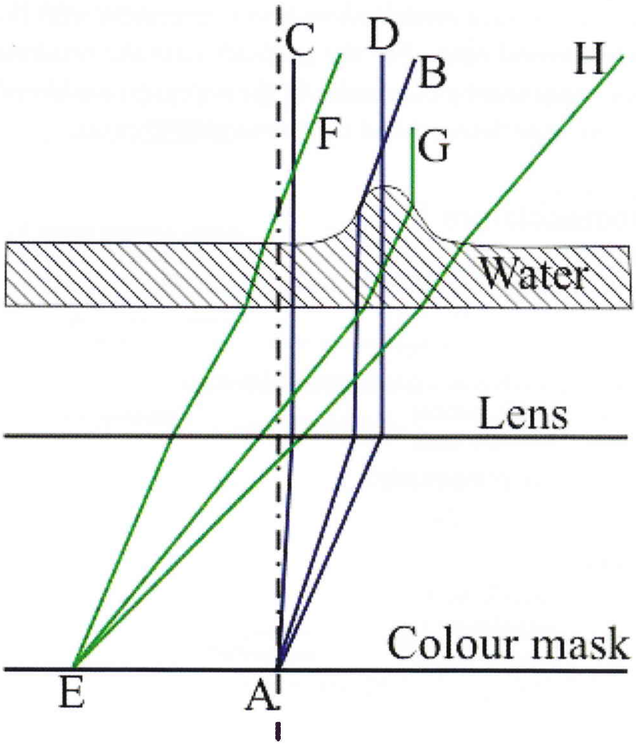

Figure 2: Principle of operation

The colour mask, made from rings of coloured cellophane, is visible as a bright circular area under the table in figure 1. It is placed on a diffusing ground glass screen positioned above four 100 W incandescent globes. An 889 mm diameter Fresnel lens is positioned just under the glass surface of the table at a distance of one focal length from the mask. In order for the camera to be positioned a large distance from the table so as to only intercept rays normal to its surface, the table was viewed through a telephoto lens after being reflected through mirrors in order to increase the distance. Three mirrors were used for the static case and five for the dynamic case; increased in the latter case to increase the field of view. The digital camera output was directed to a video recorder and a personal computer. The mask had seven colour bands and a central clear circle, each 60 mm wide. The upstream depth of the water was measured with a micrometer depth gauge. The depths for the three cases tested were, 5.1, 5.34 and 4.73 mm giving Mach/Froude numbers of 2.38, 3.12, and 4.31 respectively. Velocities were determined by measuring the time a floating particle took to travel 1 metre in the flow, taking the average of 10 readings.

Rather than having to ascertain the colour response of the camera, source mask, and light source, calibration was done directly by placing a clear plastic half cylinder, of 70 mm diameter, on the table. All slopes are represented by the half cylinder and it is only necessary to encode a particular colour with a specific range of slopes. Since a half cylinder has constant slopes along its length, each circular colour band from the colour mask is represented as two bands of colour along the length of the half cylinder; one band on either side of the centre of the cylinder. Average values of intensity were taken for the two bands of colour, and a range of intensities coupled with a range of slopes for each colour was obtained. The values were corrected for water, using the relative refractive indices of the two materials.

2.3 Free surface computation

Two types of free surface wave solution methods currently exist for the Navier-Stokes equations; interface tracking and interface capturing. The volume of fluid (VOF) method[11] is the interface capturing used in the commercial package employed in this study[12]. It allows the effects of surface tension and wall adhesion to be included. In order to handle the unsteady flow case of an accelerated wedge, as considered in this work, a code is needed which allows dynamic meshing to enable body motion within the computational domain. The technique used is known as dynamic layering.

The domain extents are $0 \leq x \leq 0.3$ m and $0 \leq y \leq 0.8$ m and $0 \leq z \leq 0.2$ m. The leading edge is 0.2 m from the origin and the width of the wedge at the trailing edge is 20 mm, half its actual width. The grid has 61435 cells in one cell zone. A structured grid is used with minimum and maximum cell volumes of 1.14×10^{-7} and $1.00 \times 10^{6}\text{m}^3$ respectively. Grid adaptation was used.

For the dynamic case a larger grid domain is required since it has to account for the entire motion of the wedge. The grid has 130210 cells in one cell zone. A structured grid is used with minimum and maximum face areas of 2.92×10^{3} and 3.00×10^{-3} m^2 respectively.

2.4 Perfect gas computation

This is done in two parts: one using a commercial CFD package[12], and the other the analytical equations for oblique shock and expansion waves, both with $\gamma = 2$. The material properties of this fictitious gas have to be entered in the code. However, γ is not entered explicitly, but rather the molecular weight and the specific heat at constant pressure are required. Neither of these two variables are known *a priori* and cannot be derived from the single value of γ. Arbitrarily the molecular weight was assumed to be that for air and the specific heat determined and then the specific heat was assumed as that for air and a different molecular weight determined. Both these cases were input as initial conditions and gave identical results. The corresponding input stagnation conditions for each Mach number could then be established assuming ambient inflow conditions.

The system is symmetric so only half the geometry is modelled. The domain extents are $-1.1 \leq x \leq 0$ m and $0 \leq y \leq 0.8$ m with flow from right to left and the origin ahead of the leading edge. The leading edge is 0.5 m from the origin and the width of the wedge at the trailing edge is 20 mm, half its actual width. The grid has 98256 cells in one cell zone. A structured grid is used with minimum and maximum face areas of 2.92×10^{-3} and 3.00×10^{-3} m^2 respectively.

In order to save computation time, the rear of the wedge was extended to the rear boundary so that the details of the wake need not be computed. This should not affect the bow and expansion wave geometry. In the analytical case the expansion wave was only taken so far as to return the flow to the free stream direction, since the actual turning angle at the rear is not known.

3. Results

The following test cases were conducted:

☐ Experimental tests on the water table.

☐ VOF method both with and without a sidewall to the computational domain, and in one case, at $Fr = 2.81$, with surface tension and wall adhesion switched off.

☐ Compressible gas with $\gamma = 2$, both analytically and with CFD.

3.1 Stationary wedge

The water table results are shown in figure 3. The strong gradients at the leading edge and tail of the model corresponding to the oblique shock and expansion fan are evident. However, the significant number of capillary waves confuses the image somewhat. Furthermore there are insufficient colour bands for accurate depth analysis. Better results could be obtained for a system with a smaller lens and much narrower colour bands in the mask, such as arranged by Skews[9]. This is a consequence in

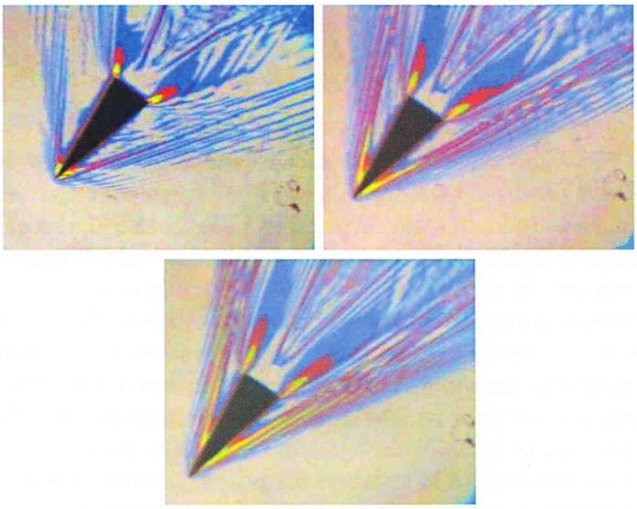

Figure 3: Experimental images from the water table, for Froude numbers of 2.38, 3.12, and 4.31

the present case of increasing the area of the Fresnel lens almost ten-fold in order to increase the field of view so as to enable dynamic wedge motion to be studied. Nevertheless quantitative results are still achievable.

The VOF solutions with an open sidewall boundary are given in figure 4. It is noted that the bow shocks are curved, particularly so for the lowest Mach number. Wave angles are thus measured closer to the wedge in order to be more in proportion to the experimental cases of figure 3. For the two stronger Mach number cases it is also noted that a dry patch is predicted in the wake region immediately behind the body. This free sidewall case results in a weak reflected wave at the wall as is to be expected.

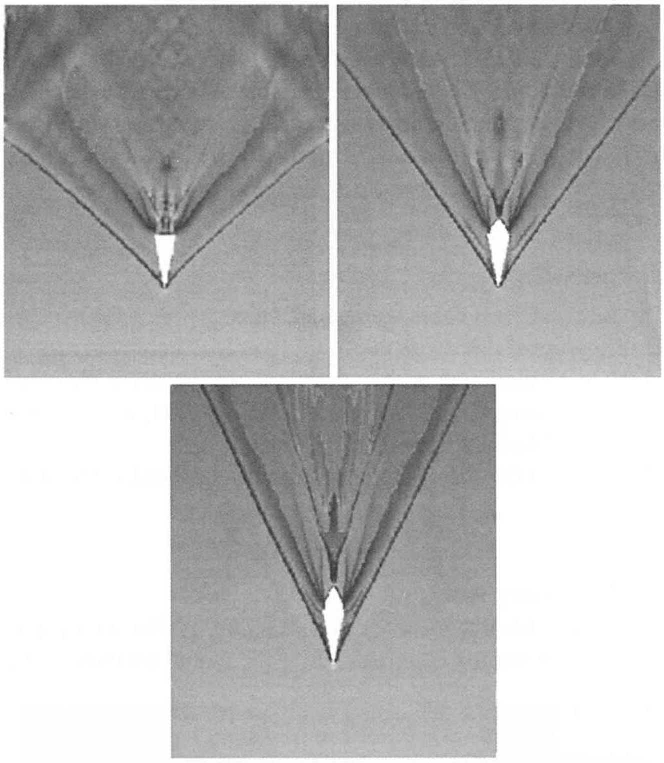

Figure 4: VOF computation without a sidewall boundary for Froude numbers of 2.38, 3.12, and 4.31

When this boundary is replaced by a wall the bow wave reflects in what appears to be a Mach reflection pattern with a small wave normal to the flow at the wall, as seen in the second image of figure 5. The third image is for the same boundary conditions as the second except that surface tension and wall adhesion are turned off in the simulation. For both these cases the water depth increases at the point of reflection to a depth greater than that of the incident jump. Furthermore there is a large convex wave which forms a short distance ahead of the outlet, nearly spanning the width of the domain, for both cases with a side wall. The cause of these waves is a mismatch in the outflow boundary condition. The outflow parameter entered was a depth, and for all cases was chosen to be the inlet depth. However this wave should not affect the upstream conditions since they are super-critical.

The effect of surface tension is evident by comparing images with and without surface tension at $Fr = 2.38$ and otherwise identical boundary conditions (second and third image in figure 5). For the no surface tension case, the flow pattern is noticeably smoother than the other two cases with surface tension at the same Froude number. For the surface tension cases, the wavelets formed due to flow interaction can be seen behind the wedge toward the end of the domain. The no surface tension case also does not have any wall adhesion, and this contributes to the dry patch behind the wedge for this case, which is not present for the other two cases at this Froude number. At higher Froude numbers all cases have the dry patch behind the wedge. This dry patch is also present in the experimental case. Surface tension effects are also more apparent in the experimental cases with more capillary waves present in all the test cases considered.

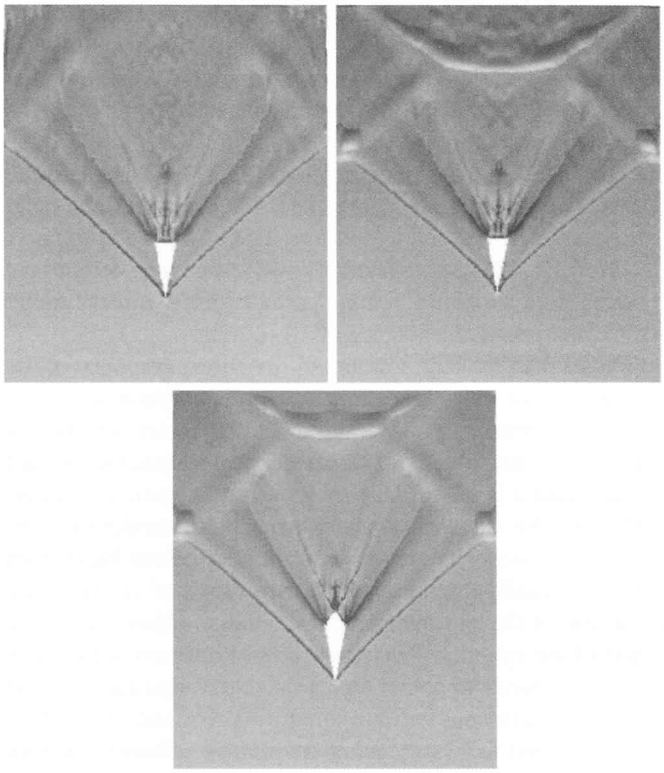

Figure 5: Comparison between Froude 2.38 VOF cases with a) no sidewall boundary, b) sidewall boundary imposed, and c) no surface tension with sidewall boundary.

Finally the results for the fictitious gas are shown in figure 6, which show conventional wave patterns for a CFD solution, the only unusual feature being that the computations are done for $\gamma = 2$.

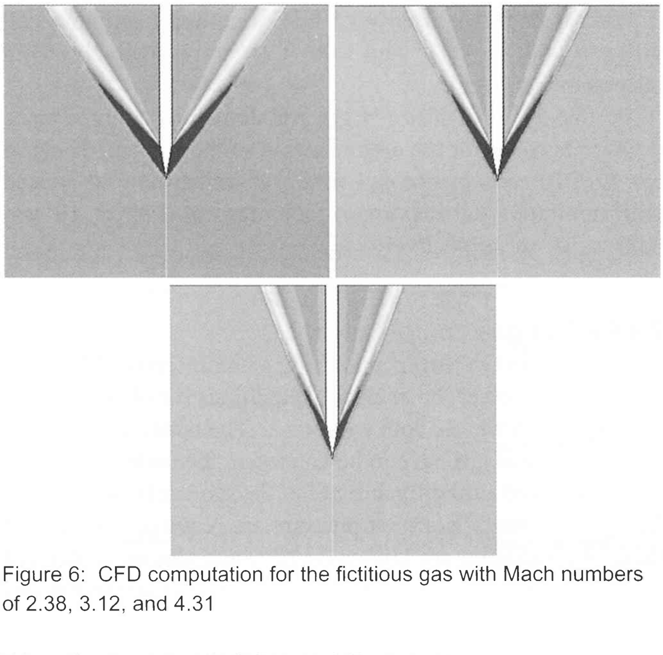

Figure 6: CFD computation for the fictitious gas with Mach numbers of 2.38, 3.12, and 4.31

The measurements of bow wave angle from the various tests for the three Mach numbers are given in table 2. Angles were measured by importing the bitmaps into a CAD software package having dimensioning options.

Froude/Mach number	2.38	3.12	4.31
Experimental	35	29	23
VOF wall	40	32	25
VOF no wall	41	30	23
VOF no surface tension	40	-	-
Gas, $\gamma = 2$, CFD	36	29	23
Gas, $\gamma = 2$, Analytical	36	29	24

Table 2: Bow wave angles

At a Froude number of 2.38, the VOF method for all the test cases over-estimates the experimental bow wave angle to a significant extent, which would be even worse if measured further from the body due to wave curvature. As the Froude numbers increase, the VOF bow wave angle estimation improves. When the Froude number increases to 3.12, the difference for both cases is 3° or less. At a Froude number of 4.31 there is agreement within measurement uncertainty. The fictitious gas case with $\gamma = 2$, shows good agreement with differences within 1°. The analytical determination of the shock angle also shows good agreement with the experimental case.

Therefore, in summary for the wave/jump angles, the analytical and fictitious gas cases show the best agreement with the experimental case across all Mach/Froude numbers. At higher Froude numbers the VOF cases show an improvement in the wave angle estimation with the experimental case. For the jump angles, there is no significant difference between the models with or without a sidewall, nor where surface tension was neglected.

In order to compare the results from the various tests, depth and density ratio profiles were analysed along a plane parallel to the free stream direction and 25 mm from the symmetry plane as shown in figure 7. The plane is 5 mm from the rear edge of the wedge (transverse to the flow), and extends 50 mm from the leading and trailing edges of the wedge. This position was chosen so that the effects of wall adhesion are not significant but that the main features are captured.

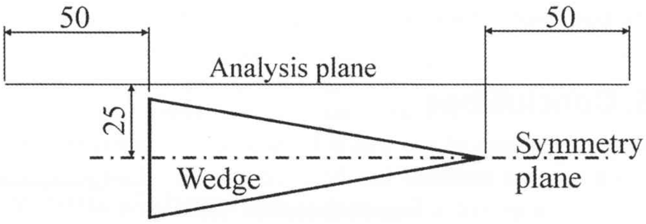

Figure 7: The plane of analysis

For the experimental results each interval of colour was measured along the profile, and the slopes determined from the calibration were used to find the heights at each interval. It is a sequential process where each height is determined from the previous height, coupled with the distance of the interval and the slope. If a colour band, e.g. red, is surrounded on both sides by another colour, e.g. blue, indicating a smaller slope, then it is assumed that a peak occurs, within that colour band, i.e. within the red colour band. The technique is not very accurate, with the limited number of bands available, and the subjective judgement to determine where the colour changes from one band to the next. An automated process with more colour bands would improve the accuracy.

Results for two of the cases (*M* & *Fr* = 2.38 and 3.12) are given in figure 8. The distance corresponding to specific bow wave angles are shown as an extra scale on the distance axis. The theoretical case is terminated when the flow through the expansion fan is turned back to the free stream direction. Since the rear of the wedge in the CFD perfect gas case is extended to the rear boundary in the computation, the data levels off prematurely because the wake is excluded.

The VOF calculations over predict the initial wave height in all cases but then settle to a plateau corresponding to the theoretical value, except the case without surface tension, after which they quite closely follow the decay due to the tail wave. Wave positions for the experimental case are reasonably well predicted but the depth in the uniform region between the bow and tail waves are not well predicted. An optical and data processing procedure of greater discrimination is required for quantitative work.

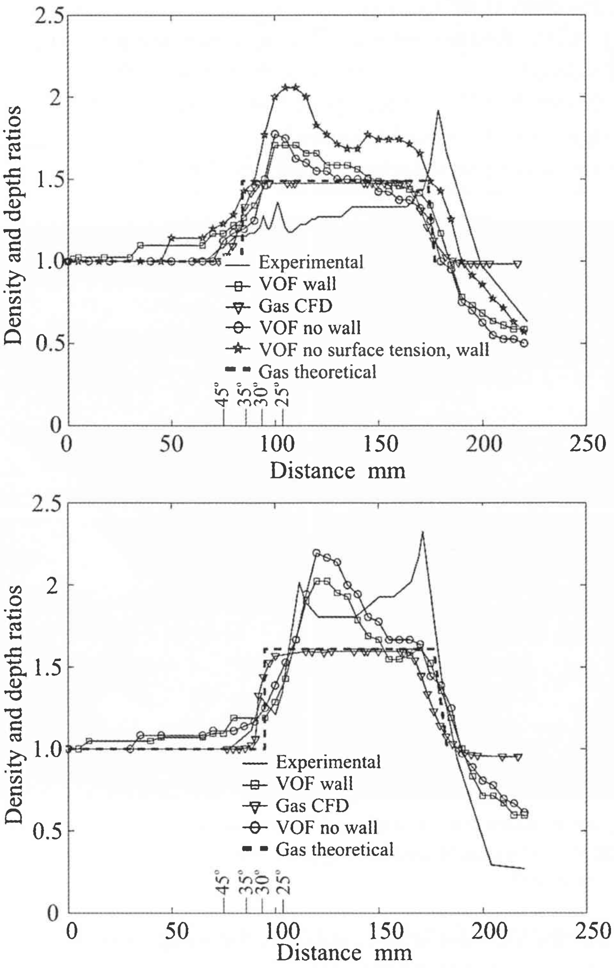

Figure 8: Depth and density variations for M & Fr = 2.38 (top) and 3.12 (bottom)

It is noted from these plots that the position of the bow wave predicted by the various methods are much more consistent with each other than is suggested by the measurements of table 2. This is because the slope of the wave starts increasing from zero ahead of the theoretical case because of the effects of surface tension in the liquid cases coupled with resolution factors in the computations. More refined calculations would improve the agreement. The same is true for the tail wave.

4. Dynamic Tests

For experimentation, the wedge is accelerated by a falling weight, connected via a pulley, with the wedge and its support running along the rail system as can be seen in figure 1. The motion is brought to rest about midway through the motion. The initial acceleration is estimated to be 7.6 m/s^2. A sequence of images for the experimental case is shown in figure 9. A limitation is that the field of view is relatively small, although larger than that for the static tests, notwithstanding the large lens used. The smallest ring diameter of the colour mask determines the area of the field of view, which is where all the colour rays overlap. To improve the situation the first few bands of colour of the colour mask could be eliminated, increasing the area left clear in the centre of the mask, but this would adversely affect the detection of low surface gradients. Once the wedge starts moving, the wave starts to form around the leading edge of the wedge (figure 9a) and only extends a short distance from it. Once the wedge has accelerated to maximum velocity, the wave is fully attached. The tail wave is also clearly discernible. When the wedge starts slowing down the bow wave starts to detach (figure 9c). As the wedge continues slowing down, the wave becomes fully detached and moves ahead of the wedge as the wave speed is greater than the wedge speed (figure 9d). By the time the wedge stops the wave has moved well ahead of the wedge and the tail wave also detaches and moves ahead of the wedge.

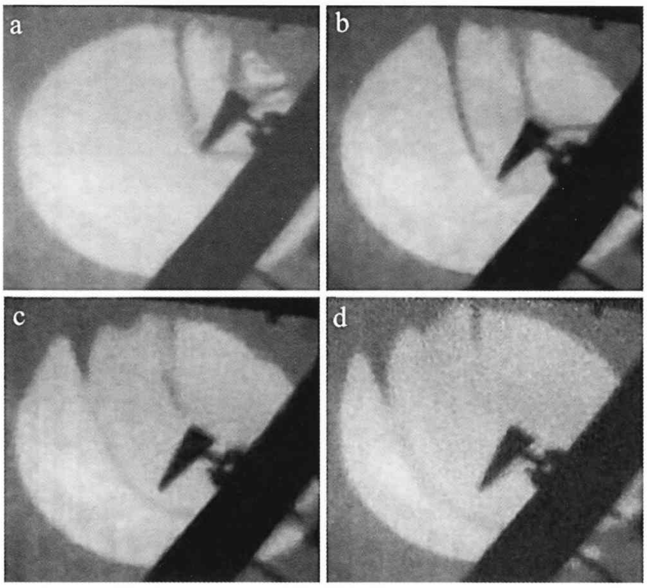

Figure 9: Experimental wave system resulting from unsteady body motion. Times measured from start of motion (s): a) 1.4, b) 1.6, c) 1.9, d) 2.0.

For the VOF dynamic simulation, the wedge was assumed to accelerate uniformly from rest to a maximum velocity of 0.66 m/s in the first 1.06 s, and then to decelerate back to zero velocity over an equal interval of time. At the start of the motion the leading edge of the wedge is 0.317 m from the rear domain boundary and 1 m from the front boundary. The distance travelled by the wedge is 0.7 m towards the front boundary before it comes to rest. It thus passes through the critical velocity ($Fr = 1$) at 0.36 and 1.42 s. Typical wave profiles are given in figure 10.

In the first image (figure 10a) the wedge has passed through supercritical velocity and the wave angle steepens when moving outward from the wedge. This results from the weaker and steeper waves from the slower earlier motion being overtaken by the stronger hydraulic jumps as the wave accelerates. Although not easily discernable no part of the perturbed field has propagated to the domain boundaries. Once the wedge has accelerated to maximum velocity, the wave is fully attached to the wedge and the wave extends to the edge of the domain (figure 10b). The tail wave is also discernible. When the wedge starts slowing down the bow wave starts to detach eventually becoming fully detached (figure 10e), and then moves ahead of the wedge as the wave speed is greater than the wedge speed. By the time the wedge stops the wave has moved well ahead of the wedge (figure 10f) and the tail wave has also detached and moved ahead of the wedge.

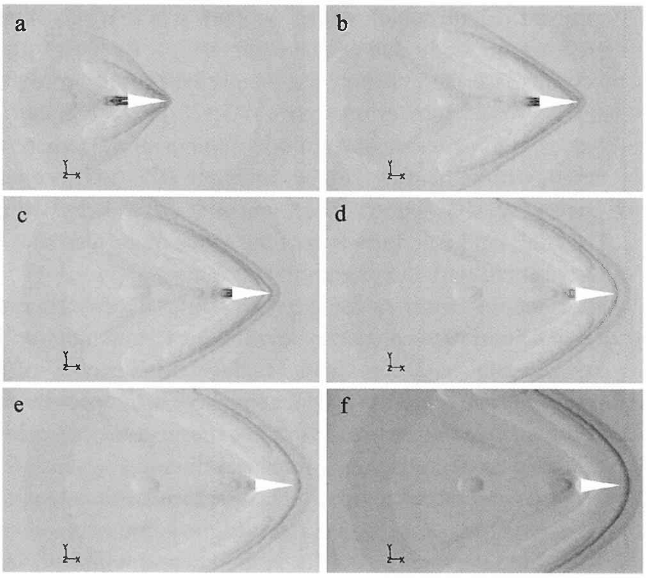

Figure 10: Wave system resulting from unsteady body motion. Times measured from start of motion (s): a) 0.99, b) 1.5, c) 1.65, d) 1.92, e) 2.01, and f) 2.1

The unsteady flow case is clearly different from the steady case as is to be expected, because even at conditions when the body has achieved super-critical velocity it is moving into a non-uniform flow field resulting from perturbations sent out ahead of the body when it was accelerating up to critical velocity.

5. Conclusions

An examination of the hydraulic analogy to supersonic flow using various methods has been conducted. Computational models comprised a free-surface flow simulation using VOF modelling and a perfect gas simulation with $\gamma = 2$. These were compared with analytical predictions and experimental results using a water table. The VOF method overestimates the bow wave angle and water depth immediately behind the wave but agreement improves with increasing Froude number. Reasonable agreement is obtained in the other cases. Quantitative comparisons of depth variation along an arbitrary line indicate that both experimental and numerical resolution need improvement. The water table technique would appear to be useful for qualitative work, particularly for unsteady flow cases which are difficult to undertake in wind tunnels where reasonable overall predictions of wave patterns are required, but its value for quantitative tests appears somewhat limited.

References

1. *Mach E*, Photography of projectile phenomena in air. *Sitzungberichte der Wiener Akademie*, 1887, 95, 164.
2. *Jouget E*, Quelque probleme d'hydrodynamic generale. *Journal de Mathematiques Pures et Appliquees*, 1920, 3.1, 1.
3. *Orlin NJ, Linder WJ and Bitterly JG*, Application of the analogy between water flow with a free surface and two-dimensional compressible gas flow, *NACA TN*. 875, 1946.
4. *Klein EJ,* Interaction of a shock wave and a wedge: an application of the hydraulic analogy, *AIAA Journal*, 1965, 3, 801-808.
5. *Mueller TJ and Oberkampf WL*, Hydraulic analog for the expansion deflection nozzle. *AIAA Journal*, 1997, 5, 1200-1202.
6. *Carbonaro M and van der Haegen V*, Hydraulic analogy to supersonic flow – lab notes, *Euroavia Symposium, Von Karman Institute for Fluid Dynamics*, Brussels, Belgium, November 2002, 1 – 9.
7. *Black J and Mediratta OP*, Supersonic flow investigations with a "hydraulic analogy" water channel, *The Aeronautical Quarterly*, 1951, 2, 27.
8. *Karelsky KV and Petrosyan AS*, Particular solutions and Riemann problem for modified shallow water equations, *Fluid Dynamics Research*, 2006, 38, 339.
9. *Skews BW*, Colour encoded visualization applied to the hydraulic analogy for supersonic flow, 1998, *8th International Symposium on Flow Visualization, Sorrento*, Italy, 31.1-31.7.
10. *Zhang X and Cox CS*, Measuring the two-dimensional structure of a wavy water surface optically: A surface gradient detector, *Experiments in Fluids*, 1994, 17, 225-237.
11. *Hirt CW and Nichols BD*, Volume of fluid method for dynamics of free boundaries, *Journal of Computational Physics*, 1981, 39, 201-221.
12. *FLUENT 6.2.16, http//:www.fluent.com, accessed 20 June 2005.*